

A component-splitting implicit time integration for multicomponent reacting flows simulations

Jingchao Zhang,¹ Jinsheng Cai,¹ and Shucheng Pan¹

School of Aeronautics, Northwestern Polytechnical University, Xi'an 710072, China

(*Electronic mail: shucheng.pan@nwpu.edu.cn)

(Dated: 7 March 2024)

A component-splitting method is proposed to improve convergence characteristics for implicit time integration of compressible multicomponent reactive flows. The characteristic decomposition of flux jacobian of multicomponent Navier-Stokes equations yields a large sparse eigensystem, presenting challenges of slow convergence and high computational costs for implicit methods. To address this issue, the component-splitting method segregates the implicit operator into two parts: one for the flow equations (density/momentum/energy) and the other for the component equations. Each part's implicit operator employs flux-vector splitting based on their respective spectral radii to achieve accelerated convergence. This approach improves the computational efficiency of implicit iteration, mitigating the quadratic increase in time cost with the number of species. Two consistency corrections are developed to reduce the introduced component-splitting error and ensure the numerical consistency of mass fraction. Importantly, the impact of component-splitting method on accuracy is minimal as the residual approaches convergence. The accuracy, efficiency, and robustness of component-splitting method are thoroughly investigated and compared with the coupled implicit scheme through several numerical cases involving thermo-chemical nonequilibrium hypersonic flows. The results demonstrate that the component-splitting method decreases the required number of iteration steps for convergence of residual and wall heat flux, decreases the computation time per iteration step, and diminishes the residual to lower magnitude. The acceleration efficiency is enhanced with increases in CFL number and number of species.

I. INTRODUCTION

In hypersonic flows, the intense shock compression and viscous dissipation lead to a substantial temperature rise, triggering chemical reactions within gas mixtures and vibrational energy excitation within molecules. Due to the comparable timescales of chemical reactions and hypersonic flows, fluid particles fail to reach a thermochemical equilibrium state before transitioning to the next position without undergoing sufficient collisions¹. Consequently, representing internal energy solely through a unified temperature becomes inadequate, necessitating the adoption of a multiple temperature model². As a result, hypersonic flows typically remain in a state of thermochemical non-equilibrium, and their numerical methods solving compressible multicomponent Navier-Stokes equations.

The multicomponent Navier-Stokes equations entail conservation equations of vibrational-electronic energy and species mass, leading to a notable increase in computational consumption compared to thermo-chemical equilibrium gases. Additionally, the disparity in time scales within flows introduces considerable numerical stiffness to the solution, exacerbating challenges related to time integration. Time integration, which involves advancing the current solution to the next time step, is typically classified into explicit, implicit, and implicit-explicit methods. Explicit integration, exemplified by backward Euler³ and multi-stage Runge-Kutta scheme⁴, offer high-order accuracy but are constrained by stability requirements dictated by the Courant-Friedrichs-Lewy (CFL) condition. Implicit integration addresses this limitation by solving the conservation equations at the implicit time level, linearizing the equations through Taylor expansion on the right-hand side at the known time level. This method provides larger time steps and achieves superlinear convergence capabilities. In the context of unsteady flow, the implicit integration can be effectively combined with the dual time-stepping⁵ and local time-stepping⁶ to attain favorable convergence rates while maintaining temporal discretization accuracy. Implicit-explicit time integration^{7,8} have been developed to leverage the strengths of both explicit and implicit methods, such as employing implicit Runge-Kutta schemes⁹ to address stiff chemistry.

The upwind spatial discretization schemes are commonly used to decompose convective fluxes into positive and negative fluxes based on the eigenvalues of the flux Jacobian matrix. Flux-difference splitting (FDS)¹⁰ and flux-vector splitting (FVS)¹¹ yields different approximations of the flux jacobian, including Roe splitting, eigenvalue splitting, and spectral radius (maximum eigenvalue) splitting. Implicit integration necessitates solving block-sparse systems, for

which two main methods exist: direct methods, such as direct inversion via Gauss elimination, and iterative methods, including relaxation iterative algorithms¹², approximation factorization decomposition¹³, and Newton-Krylov subspace methods¹⁴. While direct methods can be computationally expensive for large systems, iterative methods are commonly employed for large-scale block-sparse systems. Point relaxation and line relaxation performs symmetric Gauss-Seidel iterations in both forward and backward directions using weighted average of neighboring values, with the weighting factor determined by the specific relaxation scheme employed¹⁵. However, relaxation algorithms converge slowly or even diverge for ill-conditioned and non-diagonally dominant matrices on left-hand side. Factorization decomposition approximates the left-hand side matrix by a product of several easily invertible matrix factors, such as lower-upper symmetric Gauss-Seidel (LUSGS)¹⁶ and alternating direction implicit (ADI)¹⁷. Approximate factorization methods are more robust but introduce decomposition errors that can slow the convergence rate. Newton-Krylov subspace methods are efficient in solving large scale sparse linear systems¹⁸, with one of the most widely used applications being the generalized minimum residual (GMRES)¹⁴ method. Newton-Krylov Subspace methods necessitate an initial solution close to the converged solution, thus requiring preconditioning. The convergence acceleration of implicit integration has garnered continuous attention from researchers. Jin Yao et al.¹⁹ proposed a implicit boundary condition to introduce the flux jacobian from neighbouring multiblock for accelerated convergence of subiterative DDADI/D3ADI iteration. Zhang Rui et al.²⁰ developed conservative implicit scheme for solving the three-dimensional steady flows of molecular gases in all flow regimes from continuum one to free-molecular one. Bohao Zhou et al.²¹ proposed data-parallel upper-lower relaxation scheme based on Jacobi iteration to avoid dimensionality reduction in parallel computing, resulting in a higher convergence speed. Cao Wenbo et al.²² proposed an online dimension reduction optimization method to enhance the convergence of the traditional iterative method.

The implicit time integration encounters substantial challenges when solving multicomponent Navier-Stokes equations. One challenge from the disparity in timescale between chemical reactions and flows, while another arises from the difficulty in solving large-scale sparse matrices, impacting the convergence characteristics of implicit time integration. To enhance the computational efficiency, Gilbert Strang²³ proposed a decoupled method that separates the chemical source terms from flow equations by solving stiff ODEs, known as the Strang splitting. Dong Haibo et al.²⁴ developed a improved decoupled method which removes the standard enthalpy of formation from the total energy to thoroughly separate the effect of chemical reaction from flow equations, achieving

higher computational efficiency for reactive flows. Hansen and Sutherland²⁵ developed a robust, efficient, and adaptive dual time time-stepping technique to alleviate the time step constraint associated with ignition/extinction in the context of combustion chemistry. Xianliang Chen and Song Fu²⁶ investigated the preconditioner of GMRES in accelerating implicit time-stepping for hypersonic thermochemical nonequilibrium flows. Although the decoupled method can enhance the time step, the implicit time integration in solving multicomponent equations still face challenges in computational time and convergence. The computational complexity becomes prohibitive as the matrix dimension increases quadratically with the number of species. Wang Jian-Hang et al.²⁷ proposed a partial characteristic decomposition to improve the computational efficiency without deteriorating high-order accuracy for high-order finite difference schemes of multi-species euler equations by splitting the multicomponent eigen system into gas mixture part and species mass part. While this method addresses the issue of an exponential increase in computational cost for explicit time integration, the problem of significant computational consumption for a large number of species persists in implicit methods.

Aiming at accelerating the convergence of multicomponent Navier-Stokes equations using implicit time iteration, a component-splitting method is proposed to perform implicit iterations separately for the component conservation equations and the momentum/energy conservation equations. The left-hand side implicit operator are reformulated according to these two types of equations. The accuracy, efficiency, and robustness of this method are investigated through numerical simulations of hypersonic flows in a state of thermochemical non-equilibrium.

II. METHODOLOGY

A. Governing equations

The governing equations for the l -dimensional compressible multicomponent reactive Navier-Stokes systems are written as,

$$\frac{\partial \mathbf{Q}}{\partial t} + \frac{\partial (\mathbf{F}_{inv} + \mathbf{F}_{vis})}{\partial x_l} = \mathbf{S}, \quad (1)$$

where \mathbf{Q} , \mathbf{F}_{inv} , \mathbf{F}_{vis} , and \mathbf{S} are the vector of conservative variables, inviscid (convective) fluxes, viscid fluxes, and source term respectively, i.e.,

$$\begin{aligned}\mathbf{Q} &= [\rho, \rho u_1, \rho u_2, \rho u_3, \rho e_t, \rho e_v, \rho Y_1, \cdot, \rho Y_{ns-1}]^T \\ \mathbf{F}_{inv} &= [\rho u_l, \rho u_1 u_l + p \delta_{1,l}, \rho u_2 u_l + p \delta_{2,l}, \rho u_3 u_l + p \delta_{3,l}, \rho h u_l, \rho e_v u_l, \\ &\quad \rho Y_1 u_l, \cdot, \rho Y_{ns-1} u_l]^T \\ \mathbf{F}_{vis} &= [0, -\tau_{1,l}, -\tau_{2,l}, -\tau_{3,l}, -u_i \tau_{il} + q_l, q_{v,l}, \rho Y_1 V_{1,l}, \cdot, \rho Y_{ns-1} V_{ns-1,l}]^T \\ \mathbf{S} &= [0, 0, 0, 0, 0, \omega_v, \omega_1, \cdot, \omega_{ns-1}]^T,\end{aligned}\tag{2}$$

where $\rho, e_t, e_v, h, \omega_v$ are the density, specific total energy, specific vibrational-electronic energy, specific enthalpy, vibrational energy source, respectively. Y_s and ω_s are the mass fraction and chemical production rate of sth species, respectively. p is the pressure, δ is the kronecker delta. ns is the total number of chemical species. The density of ns th species is computed according to the conservation of mass, $Y_{ns} = 1 - \sum_{s=1}^{ns-1} Y_s$. τ_{ij} is the shear stress tensor, q_j and $q_{v,j}$ are the j -component of the translational-rotational heat flux and vibrational-electronic heat flux, $V_{s,j}$ is the diffusion velocity of sth species,

$$\tau_{il} = \mu \left(\frac{\partial u_i}{\partial x_l} + \frac{\partial u_l}{\partial x_i} \right) - \frac{2}{3} \mu \delta_{il} \frac{\partial u_k}{\partial x_k},\tag{3}$$

$$q_l = -k \frac{\partial T}{\partial x_l} + \rho \sum_{s=1}^{ns} h_s Y_s V_{s,l},\tag{4}$$

$$q_{v,l} = -k_v \frac{\partial T_v}{\partial x_l} + \rho \sum_{s=1}^{ns} e_{v,s} Y_s V_{s,l},\tag{5}$$

$$V_{s,l} = -D_s \frac{\partial Y_s}{\partial x_l},\tag{6}$$

where μ, T, T_v are viscosity, translational-rotational temperature, and vibrational-rotational temperature. k and k_v , are the thermal conductivity of T and T_v , respectively. D_s is the effective diffusion coefficient of sth species. The total energy and vibrational enthalpy are given by,

$$e_t = \frac{u_i u_i}{2} + \sum_{s=1}^{ns} h_s Y_s - \frac{p}{\rho},\tag{7}$$

$$e_v = \sum_{s=1}^{ns} e_{v,s} Y_s,\tag{8}$$

where $h_s, e_{v,s}$ are the specific enthalpy and the specific vibrational enthalpy of sth species. The ideal gas assumption is introduced to close the system,

$$p = \rho \sum_{s=1}^{ns} Y_s \frac{R_u}{M_s} T, \quad (9)$$

where R_u is the universal gas constant, M_s is the molecular weight of sth species. More detailed derivatives regarding the thermodynamic, transport, chemical reaction and vibrational excitation properties can be refer to Ref^{28,29}.

B. Implicit time integration

The governing equations are written in the generalized coordinates,

$$\frac{1}{J} \frac{\partial \mathbf{Q}}{\partial t} + \mathbf{R}(\mathbf{Q}) = 0, \quad (10)$$

where J is the determinant of the curvilinear coordinate transformation Jacobian from Cartesian coordinate (x_1, x_2, x_3) to curvilinear coordinates (ξ, η, ζ) . $\mathbf{R}(\mathbf{Q})$ is the residual associated with the spatial discretization,

$$\mathbf{R}(\mathbf{Q}) = \left(\frac{\partial \tilde{\mathbf{E}}_{inv}}{\partial \xi} + \frac{\partial \tilde{\mathbf{F}}_{inv}}{\partial \eta} + \frac{\partial \tilde{\mathbf{H}}_{inv}}{\partial \zeta} \right) + \frac{Ma}{Re} \left(\frac{\partial \tilde{\mathbf{E}}_{vis}}{\partial \xi} + \frac{\partial \tilde{\mathbf{F}}_{vis}}{\partial \eta} + \frac{\partial \tilde{\mathbf{H}}_{vis}}{\partial \zeta} \right) - \frac{1}{J} \cdot \mathbf{S}, \quad (11)$$

where $(\tilde{\mathbf{F}}_{inv}, \tilde{\mathbf{G}}_{inv}, \tilde{\mathbf{H}}_{inv})$ and $(\tilde{\mathbf{F}}_{vis}, \tilde{\mathbf{G}}_{vis}, \tilde{\mathbf{H}}_{vis})$ are the inviscid fluxes and viscous fluxes in the (ξ, η, ζ) direction, respectively. Ma and Re are the Mach number and Reynold number induced by nondimensionalization. The iteration of converging to a steady state ($\partial \mathbf{Q} / \partial t = 0$) can be accelerated by employing local time-stepping $\Delta \tau$ in replace of physical time-stepping Δt due to the fact that the choice of time step only impacts the characteristics of convergence, rather than the convergent solutions ($\mathbf{R}(\mathbf{Q}) = 0$). For unsteady solutions, the dual time-stepping is usually employed for implicit scheme,

$$\frac{1}{J} \frac{\partial \mathbf{Q}}{\partial \tau} + \frac{1}{J} \frac{\partial \mathbf{Q}}{\partial t} + \mathbf{R}(\mathbf{Q}) = 0 \quad (12)$$

where τ is the pseudo time. This dual time-stepping scheme is equal to Eq.10 when the pseudo iteration is convergent $\partial \mathbf{Q} / \partial \tau = 0$. The implicit iterate scheme of Eq. 12 in differential form is written as,

$$\left(\frac{1}{J\tau} + \frac{1+\theta}{Jt} \right) \Delta \mathbf{Q}^{m+1} = \mathbf{R}(\mathbf{Q}^{m+1}) - \frac{(1+\theta)(\mathbf{Q}^{m+1} - \mathbf{Q}^n) - \theta(\mathbf{Q}^n - \mathbf{Q}^{n-1})}{Jt}, \quad (13)$$

where $\Delta Q = Q^{m+1} - Q^m$ is the increment of the conservative variables, superscript m denotes the pseudo time level, n denotes the physical time level. θ is the time differential coefficient that $\theta = 2$ for second-order time discretization and $\theta = 0$ for first-order time discretization. $\Delta\tau$ is computed by Courant-Friedrichs-Lewy (CFL) condition,

$$\Delta\tau = \frac{J \cdot CFL}{(\lambda_{\xi,inv} + \lambda_{\eta,inv} + \lambda_{\zeta,inv}) + (\lambda_{\xi,vis} + \lambda_{\eta,vis} + \lambda_{\zeta,vis}) + \lambda_S}, \quad (14)$$

where λ is the spectral radius (maximum eigenvalue) of flux jacobian, subscript S denotes the source term. Linearizing R in Taylor expansion,

$$R(Q)^{m+1} = R(Q)^m + \left. \frac{\partial R}{\partial Q} \right|^m \Delta Q^{m+1} + O(\|\Delta Q^{m+1}\|)^2, \quad (15)$$

where $\partial R/\partial Q$ is the flux jacobian. Discarding the high-order truncation terms $O(\Delta Q^{m+1})$ in Eq.(15). Hence, the linearized implicit iteration scheme of Eq.(11) is reformulated as

$$\left(\frac{1}{J\tau} I + \frac{1+\theta}{Jt} I + \frac{\partial R}{\partial Q} \right) \Delta Q^{m+1} = R(Q^m) - \frac{(1+\theta)(Q^m - Q^n) - \theta(Q^n - Q^{n-1})}{Jt}, \quad (16)$$

where I is the identity matrix. Expanding Eq.(16) in generalized coordinates,

$$\left\{ I_m + J^{-1} \Delta\tau [\partial_\xi (A_{\xi,inv} + A_{\xi,vis}) + \partial_\eta (A_{\eta,inv} + A_{\eta,vis}) + \partial_\zeta (A_{\zeta,inv} + A_{\zeta,vis})] \right\} \Delta Q^{m+1} = LHS \Delta Q^{m+1} = RHS^m \quad (17)$$

where $\partial_\xi, \partial_\eta, \partial_\zeta$ is the differential operator in the ξ, η, ζ direction. LHS and RHS refers to the left-hand side (implicit operator) and right-hand side, in relation to convergence characteristics and spatial residuals, respectively. $A_{\xi,inv}, A_{\eta,inv}$ and $A_{\zeta,inv}$ are the flux jacobian of inviscid fluxes. $A_{\xi,vis}, A_{\eta,vis}$ and $A_{\zeta,vis}$ are the flux jacobian of viscid fluxes. A_S is the flux jacobian of source term. These formulations are given by,

$$\begin{aligned} RHS &= R - \frac{(1+\theta)(Q^m - Q^n) - \theta(Q^n - Q^{n-1})}{Jt}, I_m = \left(\frac{1}{J\Delta\tau} + \frac{1+\theta}{J\Delta t} \right) I - A_S, \\ A_{\xi,inv} &= \frac{\partial \tilde{F}_{inv}}{\partial Q}, A_{\eta,inv} = \frac{\partial \tilde{G}_{inv}}{\partial Q}, A_{\zeta,inv} = \frac{\partial \tilde{H}_{inv}}{\partial Q}, A_S = \frac{\partial S}{\partial Q}, \\ A_{\xi,vis} &= \frac{Ma}{Re} \frac{\partial \tilde{F}_{vis}}{\partial Q}, A_{\eta,vis} = \frac{Ma}{Re} \frac{\partial \tilde{G}_{vis}}{\partial Q}, A_{\zeta,vis} = \frac{Ma}{Re} \frac{\partial \tilde{H}_{vis}}{\partial Q}. \end{aligned} \quad (18)$$

The upwind spatial discretization schemes are commonly used to decompose the convective fluxes into positive and negative fluxes based on the eigenvalues of the flux Jacobian matrix, i.e., $\tilde{F}_{inv} = A Q = S^{-1} \Lambda S Q = S^{-1} (\Lambda^+ + \Lambda^-) S Q = A^+ Q_L + A^- Q_R$, where L, R denote the left and the right variables, Λ and S are the eigenvalue and eigenvector matrix calculated by characteristic decomposition. Flux-difference splitting (FDS)¹⁰ and flux-vector splitting (FVS)¹¹ generates

different approximations of flux jacobian. The first one is Roe splitting, $\mathbf{A}^\pm = (\mathbf{A} \pm |\tilde{\mathbf{A}}|)/2$, where $\tilde{\mathbf{A}}$ is the Roe averaged flux jacobian. The second one is eigenvalue splitting, $\mathbf{A}^\pm = (\mathbf{A} \pm \mathbf{S}^{-1}|\mathbf{\Lambda}|\mathbf{S})/2$. The third one is spectral splitting $\mathbf{A}^\pm = (\mathbf{A} \pm \lambda \mathbf{I})/2$, where $\lambda = \max(\text{diag}(\mathbf{\Lambda}))$ is the spectral radius of the eigenvalue matrix. The spectral splitting is widely adopted in practical applications due to its high robustness and simple formats. Then, the differential form of the convective flux jacobian matrix in ξ direction $\partial_\xi \mathbf{A}_{\xi,inv,i} = \mathbf{A}_{i+1/2} - \mathbf{A}_{i-1/2}$, resulting in

$$\mathbf{A}_{\xi,inv,i-1} = -\mathbf{A}_{i-1/2}^+, \mathbf{A}_{\xi,inv,i} = \mathbf{A}_{i+1/2}^+ - \mathbf{A}_{i-1/2}^-, \mathbf{A}_{\xi,inv,i+1} = \mathbf{A}_{i+1/2}^-. \quad (19)$$

The exact analytical form of viscous flux jacobian matrix is very complicated and is commonly approximated by viscous spectral,

$$\mathbf{A}_{\xi,vis,i-1} = -\lambda_{\xi,vis,i-1} \mathbf{I}, \mathbf{A}_{\xi,vis,i} = 2\lambda_{\xi,vis,i} \mathbf{I}, \mathbf{A}_{\xi,vis,i+1} = -\lambda_{\xi,vis,i+1} \mathbf{I}, \quad (20)$$

where $\lambda_{vis} = (\mu_l + \mu_t) \frac{Ma}{Re} \max(\frac{4\mu}{3\rho}, \frac{k}{\rho c_v}, \max_{s=1}^{ns} (D_s)) \frac{\xi_x^2 + \xi_y^2 + \xi_z^2}{J\rho}$. Similar expressions hold for the η and ζ direction. Expand Eq.17 at point (i, j, k) ,

$$\begin{aligned} & (\mathbf{I}_m + \mathbf{A}_{\xi,i} + \mathbf{A}_{\eta,j} + \mathbf{A}_{\zeta,k}) \Delta \mathbf{Q}_{ijk} + \mathbf{A}_{\xi,i+1} \Delta \mathbf{Q}_{i+1} + \mathbf{A}_{\xi,i-1} \Delta \mathbf{Q}_{i-1} + \\ & \mathbf{A}_{\eta,j+1} \Delta \mathbf{Q}_{j+1} + \mathbf{A}_{\eta,j-1} \Delta \mathbf{Q}_{j-1} + \mathbf{A}_{\zeta,k+1} \Delta \mathbf{Q}_{k+1} + \mathbf{A}_{\zeta,k-1} \Delta \mathbf{Q}_{k-1} = \mathbf{RHS}_{ijk}^m \end{aligned} \quad (21)$$

The above equation is a block sparse system and is solved by LUSGS method³⁰. The LUSGS method decomposes the LHS in Eq.21 into diagonal matrix \mathbf{D} , lower triangular matrix \mathbf{L} , and upper triangular matrix \mathbf{U} before performing a factorization,

$$\begin{aligned} & (\mathbf{D} + \mathbf{L} + \mathbf{U}) \Delta \mathbf{Q} = (\mathbf{D}(\mathbf{I} + \mathbf{D}^{-1} \mathbf{L} + \mathbf{D}^{-1} \mathbf{U})) \Delta \mathbf{Q} \\ & \approx \mathbf{D}(\mathbf{I} + \mathbf{D}^{-1} \mathbf{L})(\mathbf{I} + \mathbf{D}^{-1} \mathbf{U}) \Delta \mathbf{Q} = (\mathbf{D} + \mathbf{L}) \mathbf{D}^{-1} (\mathbf{D} + \mathbf{U}) \Delta \mathbf{Q} \end{aligned} \quad (22)$$

First, Eq.21 is solved from front to back,

$$\begin{aligned} & (\mathbf{D} + \mathbf{L}) \Delta \mathbf{Q}^{m+1,*} = \mathbf{RHS}^m, \\ & \mathbf{D} \mathbf{Q}^{m+1,*} + \mathbf{A}_{i-1} \mathbf{Q}_{i-1}^{m+1,*} + \mathbf{A}_{j-1} \mathbf{Q}_{j-1}^{m+1,*} + \mathbf{A}_{k-1} \mathbf{Q}_{k-1}^{m+1,*} = \mathbf{RHS}^m, \end{aligned} \quad (23)$$

where $\mathbf{Q}_{i-1}^{m+1,*}$, $\mathbf{Q}_{j-1}^{m+1,*}$, and $\mathbf{Q}_{k-1}^{m+1,*}$ have been solved in the previous iteration and can be moved to the right-hand side. Second, Eq.21 is solved from back to front,

$$\begin{aligned} & (\mathbf{D} + \mathbf{U}) \Delta \mathbf{Q}^{m+1} = \mathbf{D} \Delta \mathbf{Q}^{m+1,*}, \\ & \mathbf{D} \mathbf{Q}^{m+1} + \mathbf{A}_{i+1} \mathbf{Q}_{i+1}^{m+1} + \mathbf{A}_{j+1} \mathbf{Q}_{j+1}^{m+1} + \mathbf{A}_{k+1} \mathbf{Q}_{k+1}^{m+1} = \mathbf{D} \Delta \mathbf{Q}^{m+1,*}, \end{aligned} \quad (24)$$

where \mathbf{Q}_{i+1}^{m+1} , \mathbf{Q}_{j+1}^{m+1} , and \mathbf{Q}_{k+1}^{m+1} have been solved in the previous iteration and can be moved to the right-hand side.

C. Component-splitting method

The above implicit time integration uses an unified spectral radius in flux splitting, proclaimed as the coupled implicit method. However, density/momentum/energy equations and component equations have different characteristic wave speeds, i.e., different eigenvalue properties, which could impact the convergence speed. The component-splitting method separates the implicit operator into flow part solving density/momentum/energy equations and component part solving component equations. Differential flux jacobian is reformulated corresponding to flow part and component part for accelerated convergence. Different spectral radius of viscid fluxes are employed corresponding to flow equations and component equations, rather than using a unified viscous spectral. The convective flux jacobian is separated into flow part and component part, discarding the cross terms.

$$\mathbf{A}_{\xi,inv} = \frac{1}{J} \left[\begin{array}{ccccc}
 0 & \xi_x & \xi_y & \xi_z & 0 \\
 \beta E_k \xi_x - Uu & A_x & B_x & C_x & \beta \xi_x \\
 \beta E_k \xi_y - Uv & B_y & A_y & C_y & \beta \xi_y \\
 \beta E_k \xi_z - Uw & C_z & B_z & A_z & \beta \xi_z \\
 [(\gamma - 2)E_k - h]U & \varepsilon_x & \varepsilon_y & \varepsilon_z & \gamma U \\
 -Ue_v & \xi_x e_v & \xi_y e_v & \xi_z e_v & 0 \\
 -UY_1 & Y_1 \xi_x & Y_1 \xi_y & Y_1 \xi_z & 0 \\
 \dots & \dots & \dots & \dots & \dots \\
 -UY_{ns-1} & Y_{ns-1} \xi_x & Y_{ns-1} \xi_y & Y_{ns-1} \xi_z & 0 \\
 \\
 0 & 0 & \dots & 0 \\
 \Phi \xi_x & \tilde{\xi}_1 \xi_x & \dots & \tilde{\xi}_{ns-1} \xi_x \\
 \Phi \xi_y & \tilde{\xi}_1 \xi_y & \dots & \tilde{\xi}_{ns-1} \xi_y \\
 \Phi \xi_z & \tilde{\xi}_1 \xi_z & \dots & \tilde{\xi}_{ns-1} \xi_z \\
 \Phi U & \tilde{\xi}_1 U & \dots & \tilde{\xi}_{ns-1} U \\
 U & -Ue_v & \dots & -Ue_v \\
 0 & U & \dots & 0 \\
 \dots & \dots & \dots & \dots \\
 0 & 0 & \dots & U
 \end{array} \right] \quad (25)$$

where $U = u\xi_x + v\xi_y + w\xi_z + \xi_t$, $\beta = \gamma - 1$, $\Phi = -\beta + \rho_{electron}/M_{electron}$, $E_k = (u^2 + v^2 +$

$w^2)/2, \tilde{\xi}_s = \gamma RT/M_s - \beta h_s, A_x = U + (2 - \gamma)u\xi_x, B_x = -\beta v\xi_x + u\xi_y, A_y = U + (2 - \gamma)v\xi_y, B_y = -\beta u\xi_y + v\xi_x, A_z = U + (2 - \gamma)w\xi_z, B_z = -\beta v\xi_z + w\xi_y, \varepsilon_x = (E_k + h)\xi_x - \beta Uu, C_x = -\beta w\xi_x + u\xi_z, \varepsilon_y = (E_k + h)\xi_y - \beta Uv, C_y = -\beta w\xi_y + v\xi_z, \varepsilon_z = (E_k + h)\xi_z - \beta Uw, C_z = -\beta u\xi_z + w\xi_x$. Characteristic decomposition on this flux jacobian matrix generates the eigenvalue matrix $\Lambda = \text{diag}(U - c\nabla\xi, U, U, U, U + c\nabla\xi, U, \dots, U)/J$ and the spectral radius $\lambda_{inv} = |U| + c\nabla\xi$, where $\nabla\xi = \sqrt{\xi_x^2 + \xi_y^2 + \xi_z^2}$.

The implicit operator of component equations and flow equations can be independently solved without specific order. Discarding the cross effect between flow equations and component equations in implicit operator introduces component-splitting errors during iterations. Thus, all ns component equations are solved with consistence correction to address numerical inconsistencies of mass fraction.

1. Implicit operator for flow equations

The implicit operator of flow equations solves the conservative variables $\mathbf{Q}_F = [\rho, \rho u, \rho v, \rho w, \rho e]^T$ and freeze species mass fraction. The interacted flux jacobian between flow equations and component equations are neglected. Thus, the flux jacobian \mathbf{A} between convective flux and specie density is 0 and remains the upper left $[6 \times 6]$ block of Eq.25.

$$\mathbf{A} = \begin{bmatrix} 0 & \xi_x & \xi_y & \xi_z & 0 & 0 \\ \beta E_k \xi_x - Uu & A_x & B_x & C_x & \beta \xi_x & \Phi \xi_x \\ \beta E_k \xi_y - Uv & B_y & A_y & C_y & \beta \xi_y & \Phi \xi_y \\ \beta E_k \xi_z - Uw & C_z & B_z & A_z & \beta \xi_z & \Phi \xi_z \\ [(\gamma - 2)E_k - h]U & \varepsilon_x & \varepsilon_y & \varepsilon_z & \gamma U & \Phi U \\ -Ue_v & \xi_x e_v & \xi_y e_v & \xi_z e_v & 0 & U \end{bmatrix} \quad (26)$$

The spectral splitting ($\mathbf{A}^\pm = \mathbf{A} \pm \lambda \mathbf{I}$) is used to generate the differential form of the flux jacobian matrix. The spectral radius of is evaluated by $\lambda = \lambda_{inv} + \lambda_{vis}$, $\lambda_{inv} = (|U| + c\nabla\xi)/J$, $\lambda_{vis} = (\mu_l + \mu_t) \frac{Ma}{Re} \max(\frac{4\mu}{3\rho}, \frac{k}{\rho c_v}) \frac{\nabla\xi^2}{J\rho}$. Then, the differential form of the flux jacobian is

$$\mathbf{A}_{\xi,i} = (\lambda_{inv,i} + 2\lambda_{vis,i})\mathbf{I}, \mathbf{A}_{\xi,i-1} = -\mathbf{A}_{i-1/2}^+, \mathbf{A}_{\xi,i+1} = \mathbf{A}_{i+1/2}^- \quad (27)$$

2. Implicit operator for component equations

The implicit operator of component equations solves only the conservative variables $\mathbf{Q}_C = [\rho Y_1, \rho Y_2, \dots, \rho Y_{ns}]^T$ keeping \mathbf{Q}_F unchanged. Thus the flux jacobian \mathbf{A} remains the lower right $[ns - 1 \times ns - 1]$ block of Eq.25 and extends it to ns species, i.e., $U \mathbf{I}_{ns \times ns}$. The spectral radius of component equations is given by $\lambda = \lambda_{inv} + \lambda_{vis}$, $\lambda_{inv} = (|U|)/J$, $\lambda_{vis} = (\mu_l + \mu_t) \frac{Ma}{Re} \max_{s=1}^{ns} (D_s) \frac{\nabla \xi^2}{J \rho}$. The differential form of flux jacobian is given by

$$\mathbf{A}_{\xi,i} = (\lambda_{inv,i} + 2\lambda_{vis,i}) \mathbf{I}, \mathbf{A}_{\xi,i-1} = -(U_{i-1} + \lambda_i) \mathbf{I}, \mathbf{A}_{\xi,i+1} = (U_{i+1} - \lambda_i) \mathbf{I}. \quad (28)$$

Using the spectral splitting in flux splitting, the flux Jacobian matrix has all diagonal elements equal, while the off-diagonal elements are zero. In consequence, Eq.21 can be solved in scalar operation instead of matrix operation to avoid exponential increases in the computational consumption with the number of species. This makes the time cost of implicit time integration acceptable for large number of species in multicomponent equations. However, the computational cost for detailed chemistry and characteristic decomposition with large number of species remains unaffordable. A remedy for this issue can be partial decomposition²⁷ and tabulated chemistry³¹, which can be coupled with component-splitting method to solve multicomponent reactive flows.

3. Consistence correction

The coupled implicit scheme solves only $ns - 1$ component equations and uses $\rho_{ns} = \rho - \sum_{s=1}^{ns-1} \rho_s$ to avoid numerical inconsistencies of mass fraction. However, this correction is not suitable for component splitting method, as the errors accumulate in the last species. To address this issue, all ns specie equations are solved by introducing two types of consistence correction to avoid numerical inconsistencies that the total mass fraction not equaling 1. The first correction normalizes the increment of conservative variables,

$$\rho_s^{m+1} = \rho_s^m + \Delta Q_{\rho_s} + W_s (\Delta Q_{\rho} - \sum_{s=1}^{ns} \Delta Q_{\rho_s}), \quad (29)$$

where W_s is the weight coefficient, $\Delta Q_{\rho_s}, \Delta Q_{\rho}$ are the increment of specie density and total density, respectively. The weight coefficient is computed by $W_s = Q_{\rho_s} / \sum_{s=1}^{ns} \Delta Q_{\rho_s}$. Obviously, summing up the above equation yields $\rho^{m+1} = \rho^m + \Delta Q_{\rho}$, which is equivalent to the flow part. This correction only modifies the increment without altering the conservative variables at current time level, thereby ensuring conservation properties.

The second correction normalizes the specie mass fractions,

$$\rho_s^{m+1} = (\rho^m + \Delta Q_\rho) \frac{\rho_s^m + \Delta Q_{\rho_s}}{\sum_{s=1}^{ns} (\rho_s^m + \Delta Q_{\rho_s})}. \quad (30)$$

Using consistence correction finally obtains the increment of conservative variables ΔQ . Since accuracy is determined by the grid resolution, spatial discretization method, and residual magnitude, this consistence correction does not compromise the accuracy when the residual achieves convergence. In fact, it can potentially improve the accuracy by reducing the residual to lower magnitude.

III. NUMERICAL CASES

Hypersonic flows are commonly in the state of thermo-chemical non-equilibrium due to the real gas effects¹ and solve multicomponent Navier-Stokes equations for numerical simulations³². Numerical tests on hypersonic flows are conducted to assess the performance of the component-splitting method in accelerating implicit iteration. The efficiency, stability and computation time are compared between the component-splitting (CS) scheme with the coupled implicit (CI) scheme, where CS-1 and CS-2 use the first and the second consistence correction, respectively. All numerical cases employ LUSGS solving the block-sparse system and are performed on a dual-socket EPYC 7742 desktop.

A. Time acceleration test

The time acceleration ratio on implicit time integration of the CS method with respect to the number of species number is investigated through non-reactive uniform flows in a cubic box with a grid size of $10 \times 10 \times 10$, and all boundaries set to far-field equaling to the uniform flows. The chemical reaction is not considered to exclude the time cost of the detailed chemistry. The CPU time consumption of implicit time integration in a single iteration step, including assembling of flux jacobian matrix and solving the block-sparse system, is counted with the number of species increased from 16 to 4096. Let $t_{CS}(ns)$ being the CPU time consumption of implicit time integration using the CS method to solve the multicomponent equations with ns species, the growth ratio on CPU time ($t(ns)/t(16)$) and the speed-up ratio $(t_{CI}(ns) - t_{CS}(ns))/t_{CI}(ns)$ with respect to the growth ratio on the number of species ($ns/16$) are show in FIG. 1. The computation time of

the CS method is 33% and 1% of that of the CI method for 16 and 1024 species, respectively, demonstrating an acceleration in computational efficiency with increasing number of species. The time consumption of CS increases linearly with the number of species, whereas the CI method exhibits exponential growth. As a result, the CS method enhances computational efficiency and ensures the feasibility of the implicit time integration for multicomponent reactive equations when using a large number of species.

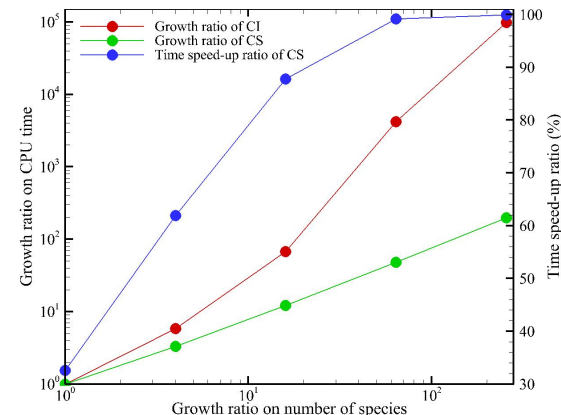


FIG. 1: Growth ratio on the CPU time and speed-up ratio with respect to the growth ratio on the number of species from $ns = 16$ to $ns = 4096$.

B. Steady hypersonic flows on cylinder

High Enthalpy Shock Tunnel Gottingen (HEG)³³ conducted several experiments on a 90mm diameter cylinder to measure the density distribution in the shock layer as well as surface pressure and heat flux. These experimental data have become a basis validation for numerical methods of thermo-chemical nonequilibrium flows. The free stream conditions are obtained from experimental inflow conditions and are presented in Table. I. Numerical simulations are performed in both 2D and 3D, where the 2D case utilized a mesh grid of 60×95 points in the circumferential and normal directions, respectively. The 3D case is conducted to simulate the experimental setup in wind tunnel with spanwise extension of 190 mm and a distance of 30 mm from the boundary. The spanwise direction is distributed with 110 grid points. The 2D and 3D computational mesh are shown in the FIG. 2. The wall boundary is assumed to be non-slip, non-catalytic, and isothermal at 300 K. The Park model² which contains 11 species with 21 elementary reactions is used to simulate chemical reactions of the air mixture with the reaction rate constants are obtained from Ref.³⁴.

The MUSCL scheme³⁵ coupled with the Roe scheme³⁶ is applied to calculate the convective flux, where the Minod limiter³⁷ is used to achieve a shock capturing capability. The Spalart-Allmaras (S-A) turbulence model³⁸ and second order central difference scheme are employed to calculate the viscous fluxes.

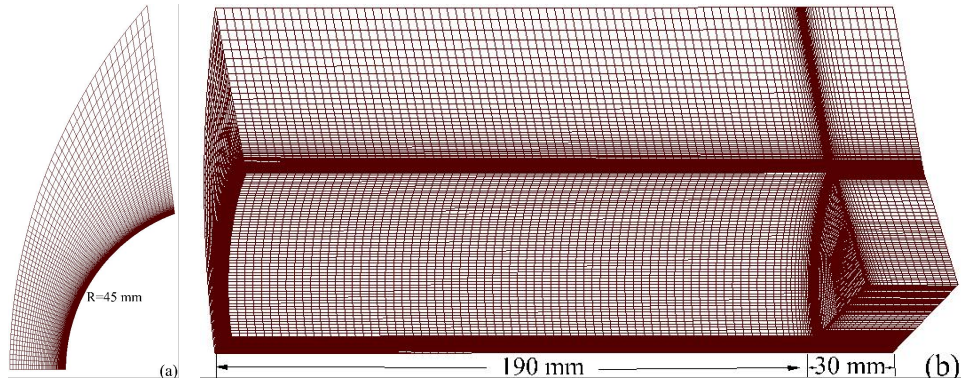


FIG. 2: Computational grid of cylinder with radius of 45 mm:(a)cylinder2D; (b)cylinder3D.

TABLE I: Free-stream conditions for numerical simulations of cylinder.

Ma	$p(\text{Pa})$	$T(\text{K})$	Y_{N_2}	Y_{O_2}	Y_N	Y_O	Y_{NO}
8.98	476	901	0.7543	0.00713	6.5×10^{-7}	0.2283	0.01026

The convergence characteristics of residual and heat flux are compared between component-splitting method and coupled implicit method. The convergence curves of residual and wall heat flux are provided in FIG. 3. In 2D simulations, the convergence criterion is set to residual magnitude reaching 10^{-1} , the CS method approximately accelerates the convergence of species density by 36.2% and 41.1% for CFL=5 and CFL=50, respectively. The convergence characteristics of the energy equation are similar to those of the component equations with the speed-up ratio is roughly equal. After considering the time consumption for flux calculations, input/output, etc., the CPU time per iteration step is reduced by 3.4%-3.6% using the CS method. With a convergence criterion of a relative error less than 1% for heat flux, the required iteration step to convergence is reduced by 54.1% and 56.5% for CFL=5 and CFL=50, respectively. In 3D simulations, the CS method can use higher CFL number for better convergence of residual of both species density and energy while diminishing the residual to lower magnitude. The computed wall heat flux at stagnation points of CS and CI, after convergence, are in close agreement with the experimental results³³,

with a relative error of approximately 6%. FIG.4 compares the wall pressure and heat flux between the results from CS, CI, and experimental data^{39,40}. In 2D simulations, due to the convergence of residual obtained from CS and CI method, errors are primarily attributed to spatial discretization. The results of the CS and CI methods are essentially identical due to the convergence of residual, indicating that the CS method does not compromise accuracy. In 3D simulations, the CS method achieves higher accuracy in wall heat flux calculations due to its lower magnitude of residual, indicating superior convergence characteristics of the component-splitting method.

C. Axisymmetric Shock-Wave Boundary Layer Interaction(ASWBLI)

NASA Turbulence Modeling Resources (TMR)⁴¹ present a basis validation for hypersonic flows. This validation is based on experiments⁴² on a cone/ogive cylinder with a radius of 10.15 cm a flare angle of 20°. The inflow conditions are summarized in TableII. The computational domain is a quarter model with $161 \times 201 \times 31$ grid points in streamwise, transverse, and circumferential direction. The wall boundary assumes non-slip, non-catalytic, and isothermal of 311K. The spatial discretization method and chemical kinetic mechanism used to calculate the residual remains consistent with the approach employed in the cylinder case. To compare the efficiency of the component-splitting method with different numbers of species, $ns = 5$ non-ionized model (N₂, O₂, NO, N, O) and $ns = 11$ ionized model (N₂, O₂, NO, N, O, NO⁺, N₂⁺, O₂⁺, N⁺, O⁺, e⁻) are used for computation.

TABLE II: Free-stream conditions for numerical simulations of ASBLI case.

Re	<i>Ma</i>	AOA(°)	<i>T</i> (K)	<i>Y</i> _{N2}	<i>Y</i> _{O2}
5.706×10^6	7.11	0.0	80	0.767	0.233

The convergence curve of residual of species density and energy are shown in FIG.5. The residual convergence behavior of the component equations is similar to that of the residual of the energy equation. In $ns = 11$ case, the CS method achieve speed-up ratio of 42.0% and 48.1% for CFL=5 and CFL=10, respectively. Larger CFL number can improve the convergence acceleration effect of component-splitting method. With the convergence criterion set as relative error less than 1%, the convergence of heat flux at stagnation points is accelerated by 42.8% and 48.0% for CFL=5 and CFL=10, respectively. Comparing the convergence curve between $ns = 11$ case

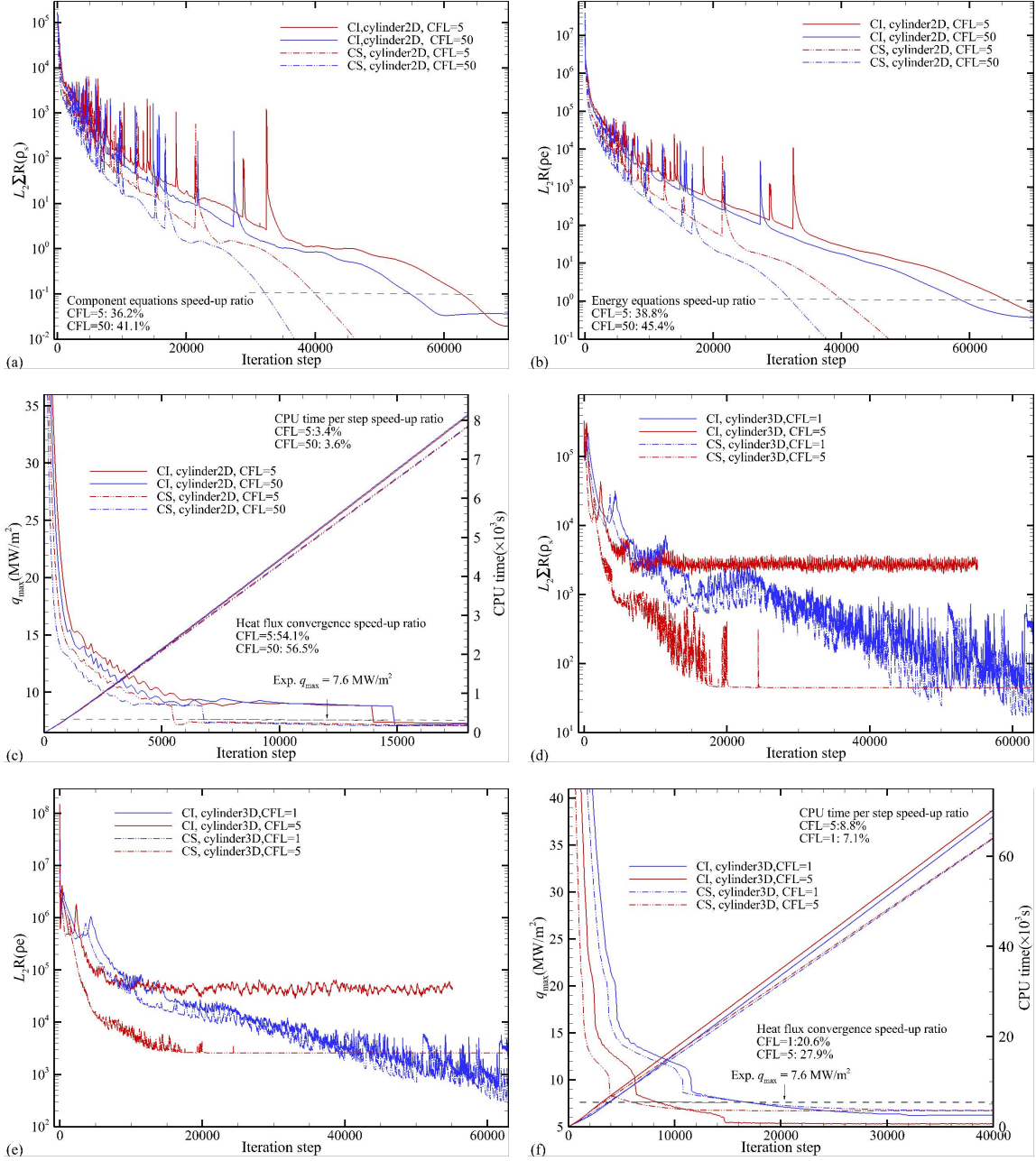


FIG. 3: Convergence curve of residual and heat flux with respect to iteration step for comparison of the CS and CI method in the cylinder case: ((a)(d)) residual of specie density; ((b)(e)) residual of energy; ((c)(f)) wall heat flux at stagnation points and CPU time cost; ((a)(b)(c)) cylinder2D; ((d)(e)(f)) cylinder3D. The dashed lines represent convergence criteria.

and $ns = 5$ case, the convergence acceleration effects of residual and heat flux are enhanced with the increase number of species. The CPU time of single step is reduced by 14.4% and 7.1% for $ns = 11$ case and $ns = 5$ case, respectively.

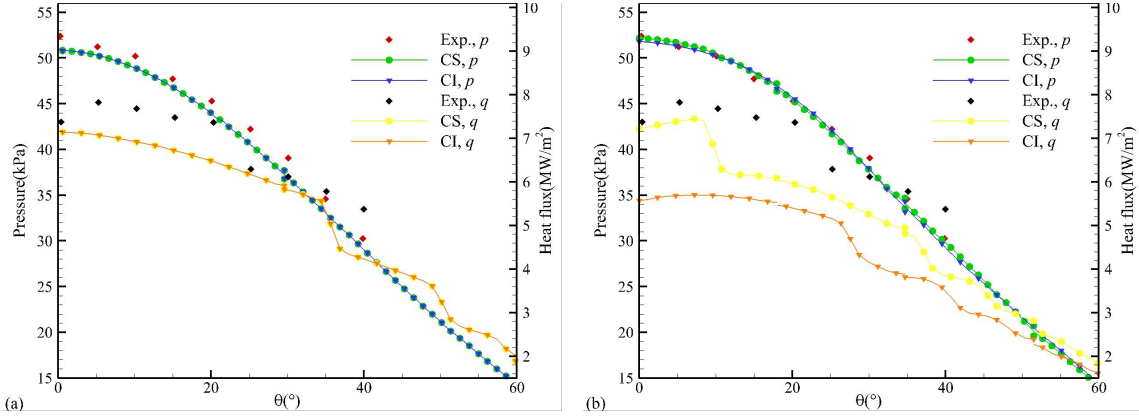


FIG. 4: Comparison of wall pressure and heat flux between CS, CI, and experimental data³⁹ for hyperersonic flows on cylinder.(a):cylinder2D;(b)cylinder3D

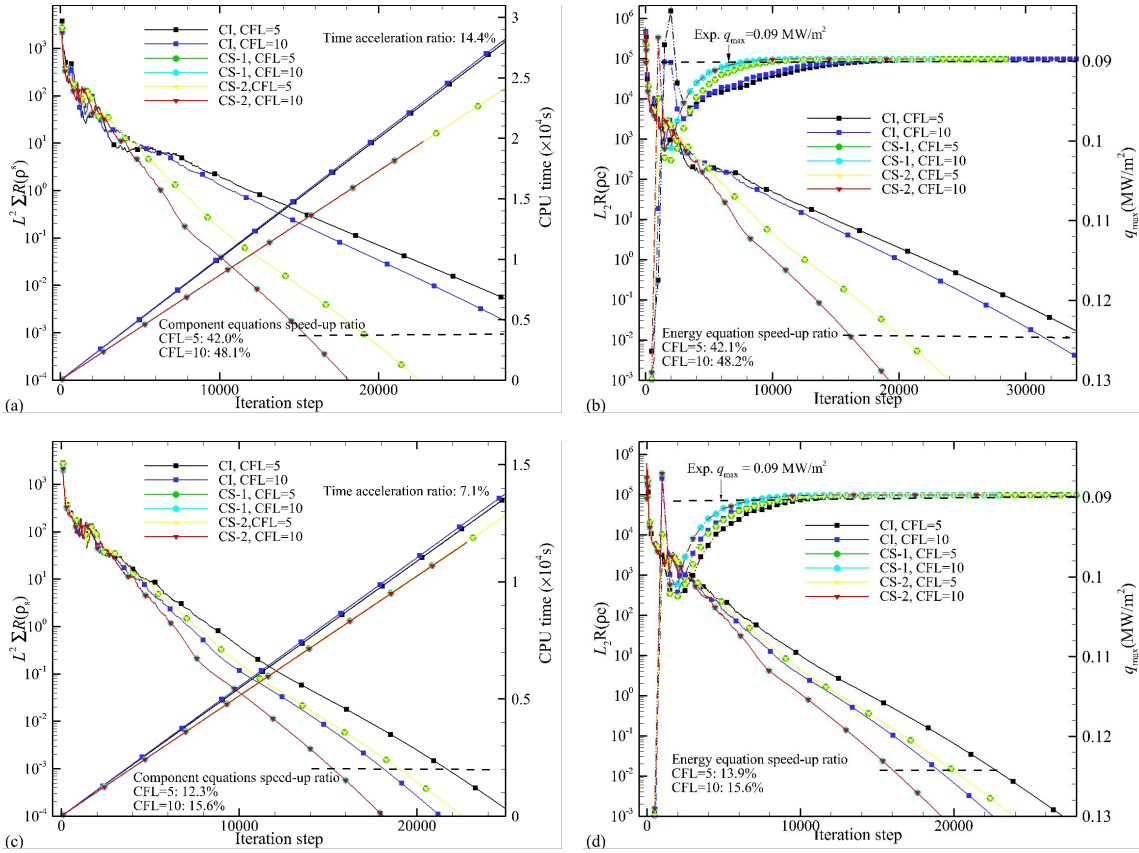


FIG. 5: Convergence curve of the residual:((a),(c)) L_2 norm of sum of residual of specie density and CPU time; ((b),(d)) L_2 norm of sum of residual of energy and wall heat flux at stagnation points;((a),(b)) $ns = 11$ case;((c),(d)) $ns = 5$ case.

The comparison of results between CS, CI, and experimental data⁴² are shown in FIG. 6. As

the residuals have all converged, there are no substantial differences between the computed results of CS and CI among different CFL numbers. In addition, the velocity profile and wall properties from simulation are in good agreement with the experimental results, validating the accuracy of numerical method spatial discretization. The pressure contour superimposed with streamlines computed by the CS method is shown in FIG. 7. An incident shock wave appears in front of the corner, followed by flow separation and the formation of a recirculation zone, before reattachment occurs. The shock wave and the boundary layer mutually interfere with each other, affecting the positions of both the shock wave and the boundary layer.

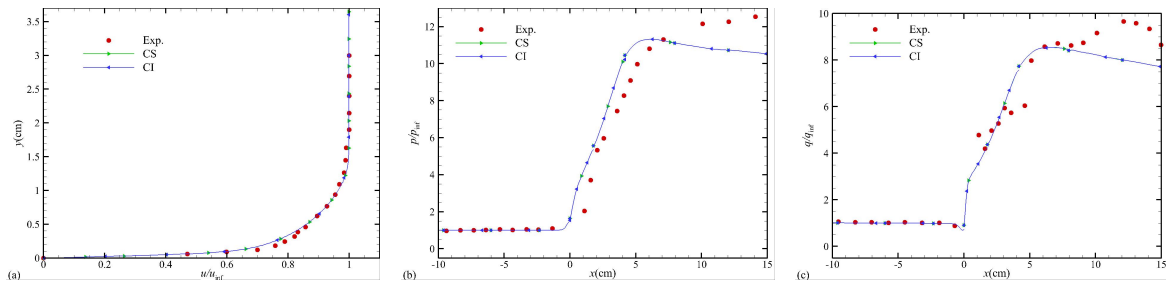


FIG. 6: Comparison of the velocity profile at $x = -6$ cm and normalized surface quantities between the CS, CI, and experimental data for the ASWBLI case:(a) normalized velocity; (b)normalized pressure; (c)normalized wall heat flux.

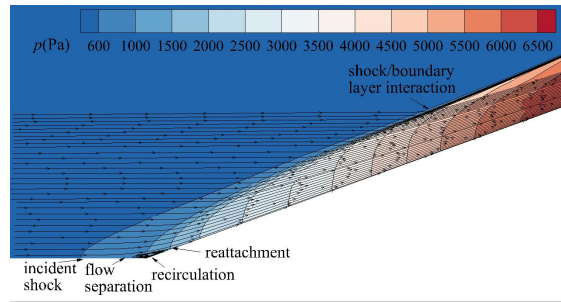


FIG. 7: Pressure contour superimposed with streamlines of the ASWBLI case calculated by the CS method.

D. Hypersonic flows of 3D capsule

The well documented generic spherical capsule (GSC)⁴³ is used here to test the component-splitting method on accelerating weakly ionized hypersonic flows. The geometry and compu-

tational grid of the GSC model are drawn in FIG. 8. The computational body-fitted grid has approximately 0.74 million finite-volume cells with a thickness of the first cell off the wall being 3.29×10^{-6} m. Two experimental states are selected for the numerical computation conditions, as shown in Table III. The spatial discretization method and chemical kinetic mechanism used to calculate the residual remains consistent with the approach employed in the cylinder case.

TABLE III: Free-stream conditions for numerical simulations of GSC reentry.

case	$u(\frac{m}{s})$	AOA($^{\circ}$)	$T(K)$	$\rho_{N_2}(\frac{kg}{m^3})$	$\rho_{O_2}(\frac{kg}{m^3})$	$\rho_{NO}(\frac{kg}{m^3})$	$\rho_O(\frac{kg}{m^3})$
case 1	2922	0.0	180	2.264E-3	6.097E-4	2.143E-4	1.505E-6
case 2	2949	28.0	191	2.431E-3	6.529E-4	2.339E-4	1.902E-6

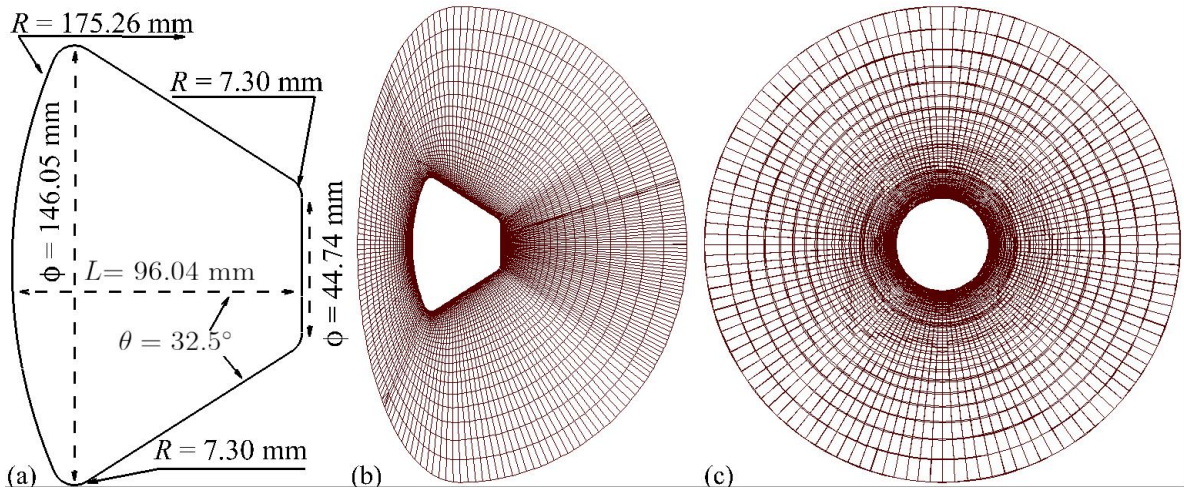


FIG. 8: (a) The geometry of the GSC vehicle; (b) the front view, and (c) the side view of the computational grid of the GSC vehicle.

The convergence curves of the residual of the species density with respect to iteration step and CPU time for the component-splitting implicit method and the coupled implicit method are shown in FIG.9. Here, the CS method achieves a reduction in computation time of single-step by approximately 6.9%. The main acceleration effect is contributed to less iteration steps to achieve convergence, especially in the large CFL number. Consequently, the required number of iterative steps for convergence of case 1 is reduced by 40.2% and 49.1% for CFL=5 and CFL=50, respectively. The acceleration ratio of case 2 was similar, and the acceleration effect was more pronounced when a large CFL number was used. In addition, the CS method converges to a lower

magnitude of the residual, resulting in higher accuracy.

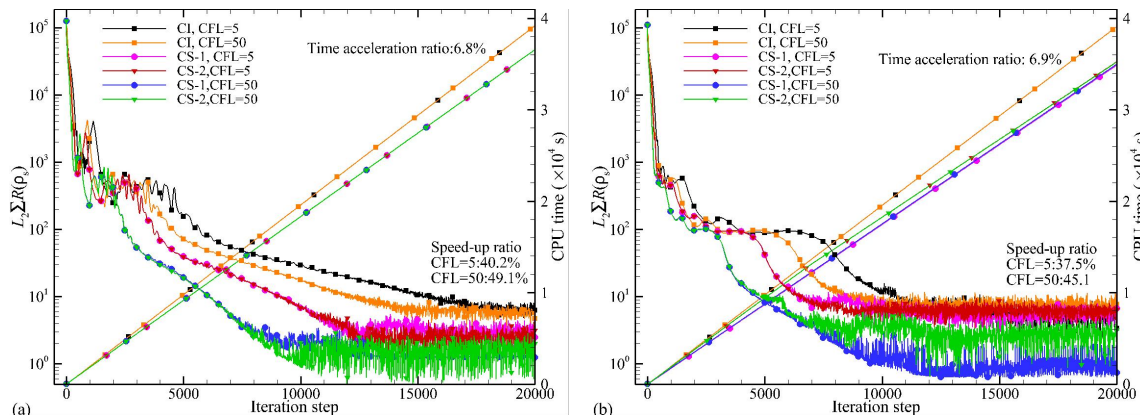


FIG. 9: Comparison of the convergence curve of L_2 norm of residual of sum of specie density with respect to iteration step and CPU time between component-splitting scheme and coupled implicit scheme for hypersonic flows of GSC reentry:(a)case 1(b)case 2.

The required number of iteration steps for the heat flux convergence in the component-splitting method and coupled implicit method are summarized in Table IV. With a convergence criterion of relative error less than 1%, the component-splitting method accelerates the convergence to heat flux at stagnation points by 50% and 66.6% for case 1 and case 2, respectively. The comparison of wall pressure and heat flux between component-splitting method and coupled implicit method with experiment results are shown in FIG. 10. The wall pressure computed by the CS and CI methods are in good agreement with experimental results, exhibiting only minor discrepancies. However, differences in wall heat flux are observed between the CS and CI methods. As the residual magnitude of the CS result is smaller, its calculated wall heat flux is more consistent with experimental results⁴³. The component-splitting method can improve the accuracy of numerical simulations by converging residuals to a lower order of magnitude.

E. Hypersonic flows of winged missile

To investigate the performance of component-splitting method in complex flows with large scale grid, numerical test is conducted on a winged missile. The geometry includes the ELECTRE blunt cone⁴⁴, a section of cone transition, a section pf cylinder, a tail rudder, and a rotating shaft, as shown in FIG. 11. The computational domain consists of structured body-fitted grid, comprising 4.6 million grid cells in half model. The free-stream condition for numerical simulation is the

TABLE IV: Comparison of iteration steps to convergence of the wall heat flux at stagnation points in the GSC cases, with a convergence criterion of relative error less than 1%.

method	case 1		case 2	
	CFL=5	CFL=50	CFL=5	CFL=50
CI	8000	6000	8000	6000
CS	6000	3000	5000	2000

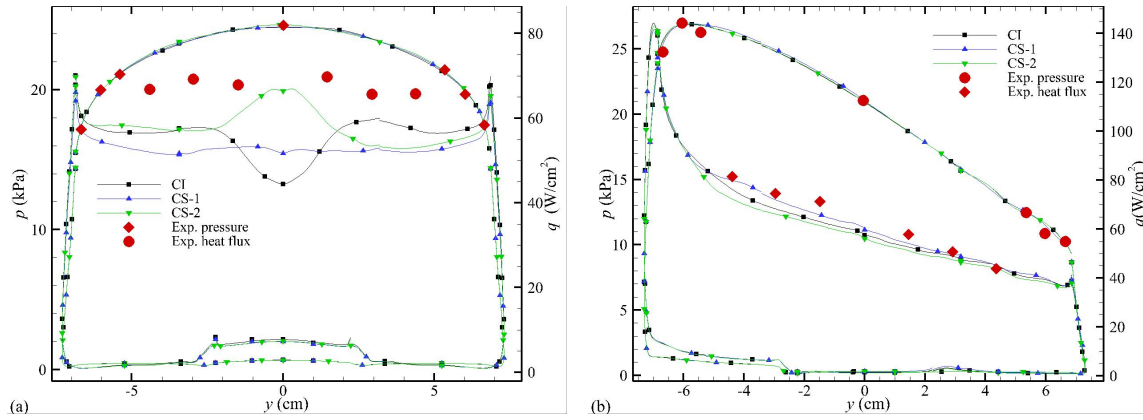


FIG. 10: Comparison of the pressure and heat flux on the surface of GSC reentry between component-splitting scheme and coupled implicit scheme:(a)case 1; (b)case 2.

atmospheric condition at altitude of 60km with a Mach number of 8. The spatial discretization method and chemical kinetic mechanism used to calculate the residual remains consistent with the approach employed in the cylinder case.

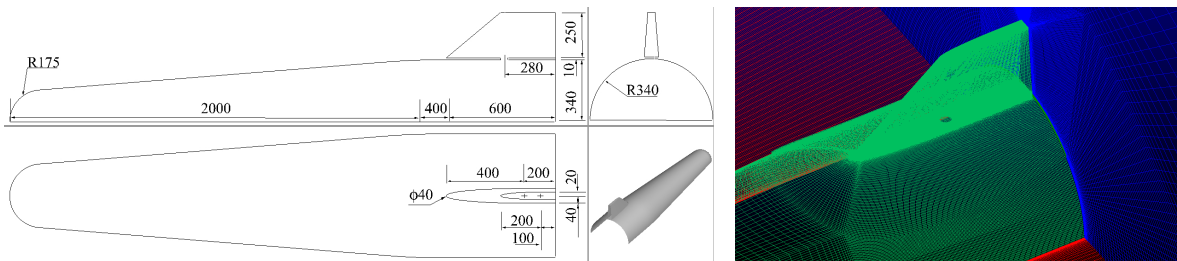


FIG. 11: Geometry and computational grid of the missile (unit:mm).

The convergence curve of heat flux at stagnation points and residual with respect to iteration steps are shown in Fig12. The component-splitting implicit method achieves substantial conver-

gence acceleration of residual and heat flux. Compared with CI method, the CS method accelerates the convergence of the residual of species density by 46.9% and 51.5% for CFL=5 and CFL=10, respectively. The convergence of heat flux and the energy equation also achieves a similar acceleration ratio. In addition, the acceleration ratio of approximately 9.4% for a single iteration step of computation also enhances the computational efficiency. As shown in FIG.13, the Mach number contour plot was computed using the CS method. The component-splitting method can effectively reduce the computational time cost for hypersonic thermochemical nonequilibrium flows.

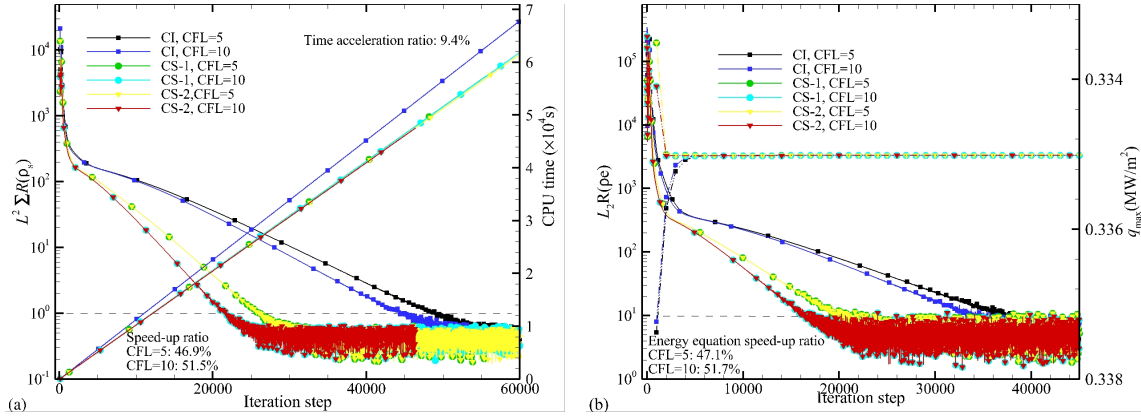


FIG. 12: Comparison of the convergence curve between CS and CI with respect to iteration step in the missile hypersonic case:(a) residual of species density and CPU time; (b)residual of energy and heat flux at stagnation points.

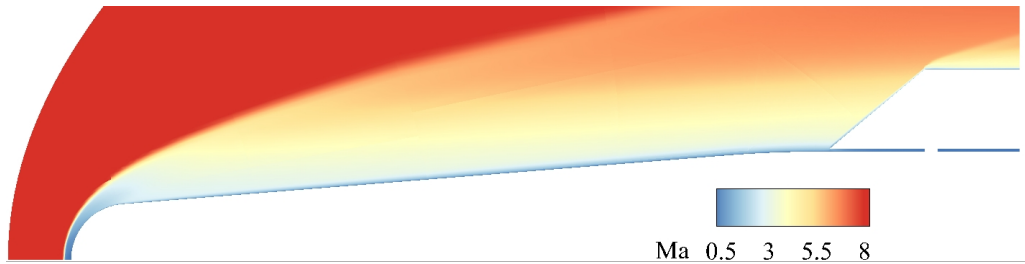


FIG. 13: Mach number contour of the missile computed by the CS method.

IV. CONCLUSION

In this paper, we propose a component-splitting method to improve the convergence characteristics of the implicit time integration for the multicomponent Navier-Stokes equations. The implicit operator is separated into the flow parts and component parts due to their distinct eigen system

of characteristic decomposition. Using corresponding spectral radius for these type equations in flux splitting to construct implicit operator achieved accelerated convergence. Two consistence corrections have been introduced to avoid the numerical inconsistencies of mass fraction. The first correction normalizes the iterative increment of the conservative variables while ensuring the conservation. The second correction normalizes the mass fraction which compromises the conservation property but achieves better robustness, resulting in higher stable CFL number. Despite compromising the conservation property, the impact of component-splitting method on accuracy is minimal when the residual reaches convergence. In addition, the flux jacobian matrix of component equations can be represented with scalar values to achieve higher computational efficiency, avoiding the computational consumption quadratically increases with the number of species. The time cost of a single implicit iteration is reduced from 33% to 99 % with the increasing number of species from 16 to 1024.

Numerical simulations on hypersonic thermo-chemical nonequilibrium flows are conducted to assess the performance of the component-splitting implicit method in solving multicomponent reactive flows. The convergence acceleration effect has two main aspects: first, the reduction of computation time for each step, and second, the reduction of iteration step to achieve convergence of residual. The component-splitting implicit method also exhibits an accelerated convergence effect in heat flux calculations. The acceleration effects are enhanced with the increasing of CFL number and species number. Lower magnitude of residual is achieved by component-splitting method indicating better accuracy and convergence characteristics. As a result, the component-splitting method can achieve better convergence characteristics for implicit time integration of multicomponent reactive flows.

ACKNOWLEDGMENTS

This work was supported by 111 project on “Aircraft Complex Flows and the Control” [grant number B17037].

DATA AVAILABILITY STATEMENT

AIP Publishing believes that all datasets underlying the conclusions of the paper should be available to readers. Authors are encouraged to deposit their datasets in publicly available reposi-

tories or present them in the main manuscript. All research articles must include a data availability statement stating where the data can be found. In this section, authors should add the respective statement from the chart below based on the availability of data in their paper.

REFERENCES

- ¹J. John D. Anderson, *Hypersonic and high temperature gas dynamics, third edition* (AIAA Education Series, 2019).
- ²C. Park, “Assessment of two-temperature kinetic model for ionizing air,” *Journal of Thermophysics and Heat Transfer* **3**, 233–244 (1989).
- ³Z. Shen, W. Yan, and G. Yuan, “A robust and contact resolving riemann solver on unstructured mesh, Part I, Euler method,” *Journal of Computational Physics* **268**, 432–455 (2014).
- ⁴A. Jameson, “Numerical solution of the euler equations for compressible inviscid fluids,” *Numerical methods for the Euler equations of Fluid Dynamics* , 199–245 (1985).
- ⁵A. Jameson, “Time dependent calculations using multigrid, with applications to unsteady flows past airfoils and wings,” in *10th computational fluid dynamics conference* (1991) p. 1596.
- ⁶J. Blazek, *Computational fluid dynamics: principles and applications*, third edition ed. (Butterworth-Heinemann, 2015) pp. 176–181.
- ⁷U. M. Ascher, S. J. Ruuth, and B. T. R. Wetton, “Implicit-explicit methods for time-dependent partial differential equations,” *SIAM Journal on Numerical Analysis* **32**, 797–823 (1995).
- ⁸L. Li and D. Xu, “Alternating direction implicit-euler method for the two-dimensional fractional evolution equation,” *Journal of Computational Physics* **236**, 157–168 (2013).
- ⁹U. M. Ascher, S. J. Ruuth, and R. J. Spiteri, “Implicit-explicit runge-kutta methods for time-dependent partial differential equations,” *Applied Numerical Mathematics* **25**, 151–167 (1997).
- ¹⁰P. Roe, “Approximate riemann solvers, parameter vectors, and difference schemes,” *Journal of Computational Physics* **135**, 250–258 (1997).
- ¹¹J. L. Steger and R. Warming, “Flux vector splitting of the inviscid gasdynamic equations with application to finite-difference methods,” *Journal of Computational Physics* **40**, 263–293 (1981).
- ¹²R. Nichols, R. Tramel, and P. Buning, “Solver and turbulence model upgrades to overflow 2 for unsteady and high-speed applications,” in *24th AIAA Applied Aerodynamics Conference* (2006).
- ¹³W. Briley and H. McDonald, “Solution of the multidimensional compressible navier-stokes equations by a generalized implicit method,” *Journal of Computational Physics* **24**, 372–397

- (1977).
- ¹⁴Y. Saad and M. H. Schultz, “GMRES: a generalized minimal residual algorithm for solving nonsymmetric linear systems,” *SIAM Journal on Scientific and Statistical Computing* **7**, 856–869 (1986).
- ¹⁵H. Lomax and J. L. Steger, “Relaxation methods in fluid mechanics,” *Annual Review of Fluid Mechanics* **7**, 63–88 (1975).
- ¹⁶S. Yoon and A. Jameson, “Lower-upper symmetric-gauss-seidel method for the euler and navier-stokes equations,” *AIAA Journal* **26**, 1025–1026 (1988).
- ¹⁷R. M. Beam and R. Warming, “An implicit finite-difference algorithm for hyperbolic systems in conservation-law form,” *Journal of Computational Physics* **22**, 87–110 (1976).
- ¹⁸D. Knoll and D. Keyes, “Jacobian-free newton-krylov methods: a survey of approaches and applications,” *Journal of Computational Physics* **193**, 357–397 (2004).
- ¹⁹Y. Jin, F. Liao, and J. Cai, “Convergence acceleration for subiterative DDADI/D3ADI using multiblock implicit boundary condition,” *Journal of Computational Physics* **429**, 110009 (2021).
- ²⁰R. Zhang, S. Liu, J. Chen, C. Zhuo, and C. Zhong, “A conservative implicit scheme for three-dimensional steady flows of diatomic gases in all flow regimes using unstructured meshes in the physical and velocity spaces,” *Physics of Fluids* **36**, 016114 (2024).
- ²¹B. Zhou, X. Huang, D. Bi, K. Zhang, and M. Zhou, “Efficient same-dimensional implicit time advancement parallel scheme and optimization methods for the iteration parameters using a graphics-processing unit,” *Physics of Fluids* **34**, 097122 (2022).
- ²²W. Cao, Y. Liu, X. Shan, C. Gao, and W. Zhang, “A novel convergence enhancement method based on online dimension reduction optimization,” *Physics of Fluids* **35**, 036124 (2023).
- ²³G. Strang, “On the construction and comparison of difference schemes,” *SIAM Journal on Numerical Analysis* **5**, 506–517 (1968).
- ²⁴H. Dong, F. Zhang, C. Xu, and J. Liu, “An improved uncoupled finite volume solver for simulating unsteady shock-induced combustion,” *Computers and Fluids* **167**, 146–157 (2018).
- ²⁵M. A. Hansen and J. C. Sutherland, “Pseudotransient continuation for combustion simulation with detailed reaction mechanisms,” *SIAM Journal on Scientific Computing* **38**, B272–B296 (2016).
- ²⁶X. Chen and S. Fu, “Convergence acceleration for high-order shock-fitting methods in hypersonic flow applications with efficient implicit time-stepping schemes,” *Computers and Fluids* **210**, 104668 (2020).

- ²⁷J.-H. Wang, S. Pan, X. Y. Hu, and N. A. Adams, “Partial characteristic decomposition for multi-species euler equations,” *Computers and Fluids* **181**, 364–382 (2019).
- ²⁸H. Su, J. Cai, K. Qu, and S. Pan, “Numerical simulations of inert and reactive highly underexpanded jets,” *Physics of Fluids* **32**, 036104 (2020).
- ²⁹P. J. Martínez Ferrer, R. Buttay, G. Lehnasch, and A. Mura, “A detailed verification procedure for compressible reactive multicomponent navier-stokes solvers,” *Computers and Fluids* **89**, 88–110 (2014).
- ³⁰S. Yoon and A. Jameson, “Lower-upper symmetric-gauss-seidel method for the euler and navier-stokes equations,” *AIAA Journal* **26**, 1025–1026 (1988).
- ³¹R. Vicquelin, B. Fiorina, S. Payet, N. Darabiha, and O. Gicquel, “Coupling tabulated chemistry with compressible cfd solvers,” *Proceedings of the Combustion Institute* **33**, 1481–1488 (2011).
- ³²X. Chen, L. Wang, and S. Fu, “Secondary instability of the hypersonic high-enthalpy boundary layers with thermal–chemical nonequilibrium effects,” *Physics of Fluids* **33**, 034132 (2021).
- ³³S. Karl, J. M. Schramm, and K. Hannemann, “High enthalpy cylinder flow in heg: A basis for cfd validation,” in *33rd AIAA Fluid Dynamics Conference and Exhibit* (2003) p. 4252.
- ³⁴P. A. Gnoffo, R. N. Gupta, and J. L. Shinn, “Conservation equations and physical models for hypersonic air flows in thermal and chemical nonequilibrium,” Tech. Rep. NASA-TP-2867 (Langley Research Center Hampton, 1989).
- ³⁵B. Van Leer, “Towards the ultimate conservative difference scheme. V. A second-order sequel to Godunov’s method,” *Journal of Computational Physics* **32**, 101–136 (1979).
- ³⁶S. Arabi, J.-Y. Trépanier, and R. Camarero, “A simple extension of roe’s scheme for multi-component real gas flows,” *Journal of Computational Physics* **388**, 178–194 (2019).
- ³⁷P. K. Sweby, “High resolution schemes using flux limiters for hyperbolic conservation laws,” *SIAM Journal on Numerical Analysis* **21**, 995–1011 (1984).
- ³⁸P. SPALART and S. ALLMARAS, “A one-equation turbulence model for aerodynamic flows,” in *30th Aerospace Sciences Meeting and Exhibit* (1992) p. 439.
- ³⁹D. Knight, J. Longo, D. Drikakis, D. Gaitonde, A. Lani, I. Nompelis, B. Reimann, and L. Walpot, “Assessment of cfd capability for prediction of hypersonic shock interactions,” *Progress in Aerospace Sciences* **48-49**, 8–26 (2012), assessment of Aerothermodynamic Flight Prediction Tools.
- ⁴⁰N. Adhikari and A. A. Alexeenko, “A general form of Macheret–Fridman classical impulsive dissociation model for nonequilibrium flows,” *Physics of Fluids* **33**, 056109 (2021).

- ⁴¹N. J. Georgiadis, C. L. Rumsey, and G. P. Huang, “Revisiting turbulence model validation for high-mach number axisymmetric compression corner flows,” in *53rd AIAA Aerospace Sciences Meeting* (2015) p. 0316.
- ⁴²M. I. Kussoy and C. C. Horstman, “Documentation of two- and three-dimensional hypersonic shock wave/turbulent boundary layer interaction flows,” Tech. Rep. NASA-TM-101075 (NASA Ames Research Center, 1989).
- ⁴³M. MacLean, E. Mundy, T. Wadhams, M. Holden, and R. Parker, “Analysis and ground test of aerothermal effects on spherical capsule geometries,” in *38th Fluid Dynamics Conference and Exhibit* (2008) p. 4273.
- ⁴⁴J. Hao, J. Wang, and C. Lee, “Numerical study of hypersonic flows over reentry configurations with different chemical nonequilibrium models,” *Acta Astronautica* **126**, 1–10 (2016).